

was nonrandom, localized to genes and within particular regions of genes, much like sense transcripts (Fig. 1 and figs. S2 and S8). This distribution is consistent with a model wherein many antisense transcripts initiate and terminate near the terminators and promoters, respectively, of the sense transcripts. Some of the apparent antisense transcripts from a gene on the plus strand could actually be sense transcripts originating from unterminated transcription of a downstream gene on the minus strand (or vice versa). However, this idea is not generally supported because there was a poor correlation between antisense tag density within a gene and the density of sense tags from the closest downstream gene (fig. S13). One explanation for the higher density of antisense tags in transcribed regions is that transcription of the sense transcripts from correct initiation sites would reduce nucleosome density throughout the entire transcribed region, thereby increasing DNA accessibility and hence the likelihood of nonspecific transcription (26). This is unlikely, given that genes with high sense tag densities did not generally have high antisense densities. There is substantial evidence that sense transcripts can be negatively regulated by antisense transcripts (3–7). Such regulation can occur either by transcriptional interference or through posttranscriptional mechanisms involving splicing or RNA-induced silenc-

ing complexes (RISCs). Our data support the possibility that antisense-mediated regulation affects a large number of genes.

References and Notes

1. P. O. Brown, D. Botstein, *Nat. Genet.* **21**, 33 (1999).
2. V. E. Velculescu *et al.*, *Cell* **88**, 243 (1997).
3. M. Lapidot, Y. Pilpel, *EMBO Rep.* **7**, 1216 (2006).
4. A. Mazo, J. W. Hodgson, S. Petruk, Y. Sedkov, H. W. Brock, *J. Cell Sci.* **120**, 2755 (2007).
5. J. A. Timmons, L. Good, *Biochem. Soc. Trans.* **34**, 1148 (2006).
6. P. Kapranov, A. T. Willingham, T. R. Gingeras, *Nat. Rev. Genet.* **8**, 413 (2007).
7. O. Yazgan, J. E. Krebs, *Biochem. Cell Biol.* **85**, 484 (2007).
8. J. Chen *et al.*, *Nucleic Acids Res.* **32**, 4812 (2004).
9. M. E. Fahey, T. F. Moore, D. G. Higgins, *Comp. Funct. Genomics* **3**, 244 (2002).
10. B. Lehner, G. Williams, R. D. Campbell, C. M. Sanderson, *Trends Genet.* **18**, 63 (2002).
11. J. Shendure, G. M. Church, *Genome Biol.* **3**, RESEARCH0044 (2002).
12. R. Yelin *et al.*, *Nat. Biotechnol.* **21**, 379 (2003).
13. H. Kiyosawa, I. Yamanaka, N. Osato, S. Kondo, Y. Hayashizaki, *Genome Res.* **13**, 1324 (2003).
14. D. J. Lipman, *Nucleic Acids Res.* **25**, 3580 (1997).
15. G. G. Carmichael, *Nat. Biotechnol.* **21**, 371 (2003).
16. RIKEN Genome Exploration Research Group and Genome Science Group (Genome Network Project Core Group) and FANTOM Consortium, *Science* **309**, 1564 (2005).
17. Y. Okazaki *et al.*, *Nature* **420**, 563 (2002).
18. D. Kampa *et al.*, *Genome Res.* **14**, 331 (2004).
19. See supporting material on Science Online.
20. A. J. Simpson, S. J. de Souza, A. A. Camargo, R. R. Brentani, *Comp. Funct. Genomics* **2**, 169 (2001).

21. B. A. Peters *et al.*, *Genome Res.* **17**, 287 (2007).
22. M. Sultan *et al.*, *Science* **321**, 956 (2008); published online 3 July 2008 (10.1126/science.1160342).
23. A. Mortazavi, B. A. Williams, K. McCue, L. Schaeffer, B. Wold, *Nat. Methods* **5**, 621 (2008).
24. J. Q. Wu *et al.*, *Genome Biol.* **9**, R3 (2008).
25. J. M. Johnson, S. Edwards, D. Shoemaker, E. E. Schadt, *Trends Genet.* **21**, 93 (2005).
26. K. Struhl, *Nat. Struct. Mol. Biol.* **14**, 103 (2007).
27. We thank W. Yu for assistance with microarrays. Supported by the Virginia and D. K. Ludwig Fund for Cancer Research and NIH grants CA57345, CA43460, CA62924, and CA121113. Under a licensing agreement between Johns Hopkins University and Genzyme, technologies related to SAGE were licensed to Genzyme for commercial purposes, and B.V., V.E.V., and K.W.K. are entitled to a share of the royalties received by the university from the sales of the licensed technologies. The university and researchers (B.V. and K.W.K.) own Genzyme stock, which is subject to certain restrictions under university policy. The terms of these arrangements are being managed by the university in accordance with its conflict-of-interest policies. There are existing patents for SAGE that have been licensed as disclosed above, and similar patents are likely to be filed for ASSAGE.

Supporting Online Material

www.sciencemag.org/cgi/content/full/1163853/DC1

Materials and Methods

Figs. S1 to S13

Tables S1 to S3

References

26 July 2008; accepted 10 November 2008

Published online 4 December 2008;

10.1126/science.1163853

Include this information when citing this paper.

Label-Free Biomedical Imaging with High Sensitivity by Stimulated Raman Scattering Microscopy

Christian W. Freudiger,^{1,2*} Wei Min,^{1*} Brian G. Saar,¹ Sijia Lu,¹ Gary R. Holtom,¹ Chengwei He,³ Jason C. Tsai,⁴ Jing X. Kang,³ X. Sunney Xie^{1†}

Label-free chemical contrast is highly desirable in biomedical imaging. Spontaneous Raman microscopy provides specific vibrational signatures of chemical bonds, but is often hindered by low sensitivity. Here we report a three-dimensional multiphoton vibrational imaging technique based on stimulated Raman scattering (SRS). The sensitivity of SRS imaging is significantly greater than that of spontaneous Raman microscopy, which is achieved by implementing high-frequency (megahertz) phase-sensitive detection. SRS microscopy has a major advantage over previous coherent Raman techniques in that it offers background-free and readily interpretable chemical contrast. We show a variety of biomedical applications, such as differentiating distributions of omega-3 fatty acids and saturated lipids in living cells, imaging of brain and skin tissues based on intrinsic lipid contrast, and monitoring drug delivery through the epidermis.

Vibrational microscopies based on infrared absorption and Raman scattering (1, 2) have been used as label-free contrast mechanisms due to characteristic frequencies of various chemical bonds. However, infrared microscopy has limited spatial resolution because of long infrared wavelengths. Spontaneous Raman scattering microscopy, while having higher spatial resolution due to shorter excitation wavelengths, is insensitive and thus often has limited imaging speed. Coherent anti-Stokes Raman scattering (CARS) microscopy offers higher sensitivity than spontaneous Raman microscopy (3, 4). However, a CARS spectrum is different from its corresponding spontaneous Raman spectrum due to a nonresonant background, which complicates spectral assignment, causes difficulties in image interpretation, and limits detection sensitivity.

Here we explore stimulated Raman scattering (SRS) as an imaging contrast mechanism. SRS is analogous (5, 6) to the well-known phenomenon of stimulated emission (7) and was first observed

in 1962 (8). Since then it has been used in many spectroscopic studies (9–12). In spontaneous Raman scattering, one laser beam at a frequency ω_p illuminates the sample and the signal is generated at the Stokes and anti-Stokes frequencies, ω_S and ω_{AS} , respectively, due to inelastic scattering. In SRS, however, two laser beams at ω_p and ω_S coincide on the sample (Fig. 1A). When the difference frequency, $\Delta\omega = \omega_p - \omega_S$, also called the Raman shift, matches a particular molecular vibrational frequency Ω , amplification of the Raman signal is achieved by virtue of stimulated excitation. Consequently, the intensity of the Stokes beam, I_S , experiences a gain, ΔI_S (stimulated Raman gain, SRG), and the intensity of the pump beam, I_p , experiences a loss, ΔI_p (stimulated Raman loss, SRL), as shown in Fig. 1B. In contrast, when $\Delta\omega$ does not match any vibrational resonance, SRL and SRG cannot occur. Therefore, unlike CARS, SRL and SRG do not exhibit a nonresonant background (11).

The intensity of SRG or SRL is described by $\Delta I_S \propto N \times \sigma_{\text{Raman}} \times I_p \times I_S$ and $\Delta I_p \propto -N \times$

¹Department of Chemistry and Chemical Biology, Harvard University, Cambridge, MA 02138, USA. ²Department of Physics, Harvard University, Cambridge, MA 02138, USA.

³Department of Medicine, Massachusetts General Hospital and Harvard Medical School, Boston, MA 02114, USA.

⁴Pfizer Global Medical, 685 3rd Avenue, MS 1325, New York, NY 10017, USA.

*These authors contributed equally to this work.

†To whom correspondence should be addressed. E-mail: xie@chemistry.harvard.edu

$\sigma_{\text{Raman}} \times I_p \times I_s$, where N is the number of molecules in the probe volume and σ_{Raman} is the molecular Raman scattering cross-section (6). As in other multiphoton techniques (3, 13), the nonlinearity of SRL and SRG in the overall excitation intensity allows three-dimensional (3D) sectioning. Such nonlinear excitation is typically accomplished by picosecond or femtosecond pulse trains in the near-infrared region.

SRS as a contrast mechanism for microscopy has been recently reported using multiplex detection with a photodiode array in combination with a femtosecond amplified laser system (14). Although the amplified laser system generates a large SRS signal, it is not suitable for bioimaging because the excessive peak power causes sample damage (15) and the low repetition rate limits the image acquisition speed.

We take a different approach, using high-repetition rate (76 MHz) picosecond pulse trains with more than three orders of magnitude lower peak power. The pump beam for SRL is provided by a synchronously pumped, tunable optical parametric oscillator (OPO), and the Stokes beam is provided by a 1064-nm mode-locked Nd:YVO₄ oscillator. A 7-ps pulse width is chosen because its frequency bandwidth offers optimal spectral resolution (3 cm⁻¹). Under this excitation condition, the small SRL and SRG signals ($\Delta I_p/I_p$ and $\Delta I_s/I_s < 10^{-4}$) are buried in the laser noise. Realizing that laser noise occurs primarily at low frequencies, we implement a high-frequency phase-sensitive detection scheme, as previously used in other applications (10, 16, 17). For SRL, we modulate the intensity of the Stokes beam at 1.7 MHz and detect the resulting intensity modulation of the pump beam at the same frequency with a lock-in amplifier (Fig. 1C). Similarly, SRG can be measured by modulating the pump beam and detecting the Stokes beam (18). With this approach, $\Delta I_p/I_p < 10^{-7}$ can be achieved with a 1-s time constant. To acquire images via beam scanning, we used a 300- μ s time constant and a pixel dwell time of 170 μ s. It is difficult to incorporate such phase-sensitive detection at radio frequency (MHz) with a multiplex detector such as a diode array. Our approach can detect intensity changes $\Delta I_p/I_p$ and $\Delta I_s/I_s$ four orders of magnitude more sensitive than in the previous report (14).

Collinear pump and Stokes beams are focused with a high-numerical aperture (NA) objective (NA = 1.2) onto a common focal spot (Fig. 1D). In SRS, the spatial resolution is diffraction limited and similar to that of two-photon fluorescence. Because SRL and SRG are measured at the same frequencies as those of the input fields, phase matching is automatically fulfilled. This allows deconvolution with a point spread function similar to that of fluorescence microscopy and makes image interpretation simpler than in the case of CARS (19).

To detect the pump or Stokes beams in the forward direction, we used a condenser with an NA = 1.35, which is higher than that of the excitation objective, to minimize spurious back-

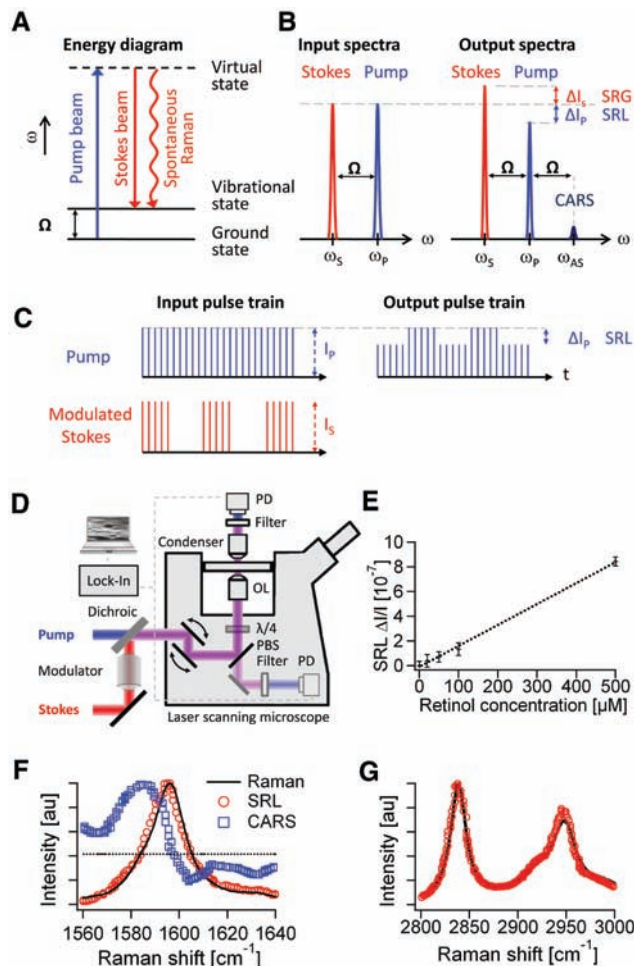
ground due to cross-phase modulation (20, 21). Alternatively, backward (epi) detection is possible in turbid samples because multiple scattering events redirect a considerable portion of the forward-propagating pump and Stokes beams to the backward direction, which can be collected with the same excitation objective lens (22). SRL or SRG spectra at a particular position in the sample can be recorded by automated OPO tuning. We detected SRL instead of SRG because the responsivity of the photodiode used is higher for the pump than for the Stokes beam.

We verified that SRL is linear in both I_p and I_s (18). Unlike the CARS signal that is proportional to the square of the concentration, the linear dependence of SRL on analyte concentration (Fig. 1E) allows straightforward quantitative analysis. The detection limit is 50 μ M for retinol (Fig. 1E) and 5 mM for methanol

solutions (18), with average laser power <40 mW (30 MW/cm²) for each beam. Close to the shot noise limit, this sensitivity corresponds to about 3000 retinol and 300,000 methanol molecules in focus, respectively, which has surpassed the detection limit reported for CARS microscopy (23).

We show in Fig. 1F the SRL, spontaneous Raman, and CARS spectra of an isolated Raman peak of *trans*-retinol (18). Whereas SRL and spontaneous Raman spectra are nearly identical, the CARS spectrum exhibits a nonresonant background independent of the Raman shift, and spectral distortion because of interference with the background (24). Good agreement between the SRL, SRG, and spontaneous Raman spectra is also seen for spectra with multiple peaks (Fig. 1G) (18, 25). Thus, SRS allows simple spectroscopic identification based on the Raman literature, particularly in the “crowded” fingerprint region.

Fig. 1. Principle and design of SRS microscopy. **(A)** Energy diagram for SRS. **(B)** Input and output spectra of SRS. SRS leads to an intensity increase in the Stokes beam (SRG) and an intensity decrease in the pump beam (SRL). Also shown (not to scale) is the CARS signal generated at the anti-Stokes frequency ω_{AS} . **(C)** SRL detection scheme. Stokes beam is modulated at high frequency (MHz), at which the resulting amplitude modulation of the pump beam due to SRL can be detected. **(D)** SRL microscope with both forward and epi detection. The Stokes beam is modulated by an electro-optic modulator. The transmitted or reflected pump beam is filtered and detected by a large-area photodiode (PD). For epi detection, the back-scattered beams are collected by the excitation objective lens (OL) and separated from the excitation beams by a combination of a quarter wave plate ($\lambda/4$) and polarizing beam splitter (PBS). The SRL is measured by a lock-in amplifier to provide a pixel of the image. Three-dimensional images are obtained by raster-scanning the laser focus across the sample, and microspectroscopy can be performed by automated tuning of the pump wavelength. **(E)** Linear dependence of SRL on concentrations of retinol in ethanol at 1595 cm⁻¹. Modulation depth $\Delta I_p/I_p < 10^{-7}$ can be achieved. Error bars show 1 SD of the signals for a 1-min recording. The detection limit was determined to be 50 μ M. **(F)** Agreement of SRL spectrum (red circles) with the spontaneous Raman spectrum (black line) of the Raman peak (1595 cm⁻¹) of 10 mM retinol in ethanol. The distorted CARS spectrum (blue squares) exhibits a typical peak shift, dispersive shape and nonresonant background. **(G)** Agreement of the more complex SRL spectrum of methanol (red circles) with the spontaneous Raman spectrum (black line).



As the first application, we monitored the uptake of omega-3 fatty acids by living human lung cancer cells through SRL imaging and microspectroscopy (Fig. 2). Polyunsaturated omega-3 fatty acids, such as eicosapentaenoic acid (EPA), provide health benefits through mechanisms such as dampening inflammation, lowering blood tri-

glyceride concentrations, and inducing cancer cell apoptosis, but can only be obtained from the diet (26). As shown in Fig. 2A, unsaturated fatty acids exhibit a Raman band at 3015 cm^{-1} , attributable to the stretching mode of $=\text{C}-\text{H}$ bond associated with $\text{C}=\text{C}$ double bonds (27). The intensity of this 3015 cm^{-1} mode is approximately

proportional to the number of $\text{C}=\text{C}$ double bonds in the lipid molecule. In contrast, the 2920 cm^{-1} peak intensity is found to be similar for all saturated and unsaturated fatty acids.

When cells are grown with $25\text{ }\mu\text{M}$ EPA for 24 hours (18), lipid droplets (LDs) are visible when imaging at both 2920 cm^{-1} (Fig. 2C) and 3015 cm^{-1} (Fig. 2D) bands. The SRL images show a much stronger signal outside the LDs at 2920 cm^{-1} than at 3015 cm^{-1} , indicating that most of the fatty acids outside the LDs are saturated. In the absence of EPA in the culturing media, the cells have few LDs inside the cytoplasm due to the limited lipid supply (18). We also conducted SRL microspectroscopy at specific positions inside the cell to identify the local chemical composition. The nucleus exhibits an SRL spectrum (blue in Fig. 2B) similar to that of the saturated fatty acids, with negligible contribution at 3015 cm^{-1} , whereas the spectrum from the LD has a pronounced 3015 cm^{-1} peak (red in Fig. 2B). No sign of photodamage, such as plasma membrane blebbing (15), was observed after repeated images of the same cell. Therefore, we can use SRL spectral imaging and microspectroscopy to follow uptake of unsaturated fatty acids by living cells, opening possibilities to study lipid metabolism and its associated diseases.

Next, we present SRS tissue imaging without staining. Many stains are impossible to apply in vivo. Label-free optical techniques, such as optical coherence tomography and diffusive optical tomography, often do not offer chemical contrast, while autofluorescence is limited to a few chemical species. A strong SRL signal originates from the CH_2 stretching vibration (2845 cm^{-1}) of lipids in tissue, especially in the brain, where lipid-rich myelin sheaths surround axons, as was seen in CARS microscopy (28). Figure 3A shows forward-detected SRL images of a fiber tract in the corpus callosum of a thin slice of mouse brain. We also demonstrate epi SRL imaging from a $\sim 1\text{-mm}$ -thick slice of mouse brain (Fig. 3B), which clearly reveals individual neurons.

Skin imaging is another application of SRS microscopy. Figure 3C shows three individual SRL sections of mouse skin in the same area but at different depths, all with $\Delta\omega$ tuned into 2845 cm^{-1} (18). This highlights the 3D sectioning capability and subcellular resolution of SRS in tissue. At a depth of $4\text{ }\mu\text{m}$, the SRL image shows the stratum corneum, which consists of polygonal cells and serves as the main protective layer of the body. This suggests that the intercellular space is rich in lipids. At a depth of $42\text{ }\mu\text{m}$, lipid-rich sebaceous glands can be identified in the dermis. The nuclei of the gland cells are dark spots due to the lack of lipids. At a depth of $105\text{ }\mu\text{m}$, the subcutaneous fat layer is clearly visible.

Figure 3D compares on and off vibrational resonance SRL and CARS images of stratum corneum. When $\Delta\omega$ is tuned from on-resonance (2845 cm^{-1}) to off-resonance (2780 cm^{-1}) of the

Fig. 2. Omega-3 fatty acid uptake by A549 human lung-cancer cells monitored with SRL microscopy and microspectroscopy. (A) Spontaneous Raman spectra of docosahexaenoic acid (DHA, with six $\text{C}=\text{C}$ bonds), eicosapentaenoic acid (EPA, with five $\text{C}=\text{C}$ bonds), arachidonic acid (AA, with four $\text{C}=\text{C}$ bonds), and oleic acid (OA, with a single $\text{C}=\text{C}$ bond). The strong Raman peak around 3015 cm^{-1} is characteristic of unsaturated fatty acids. (B) SRL spectra of a lipid droplet (LD, red line) and a region inside the nucleus (blue line). Unlike the nuclear region, the SRL spectrum of the LD shows good correspondence with the spectra from the pure EPA shown in (A). (C) SRL image of a cell at 2920 cm^{-1} . (D) SRL image of the same cell at 3015 cm^{-1} . These findings indicate that EPA is taken up by the cells and more strongly enriched in the LDs compared to other cellular organelles.

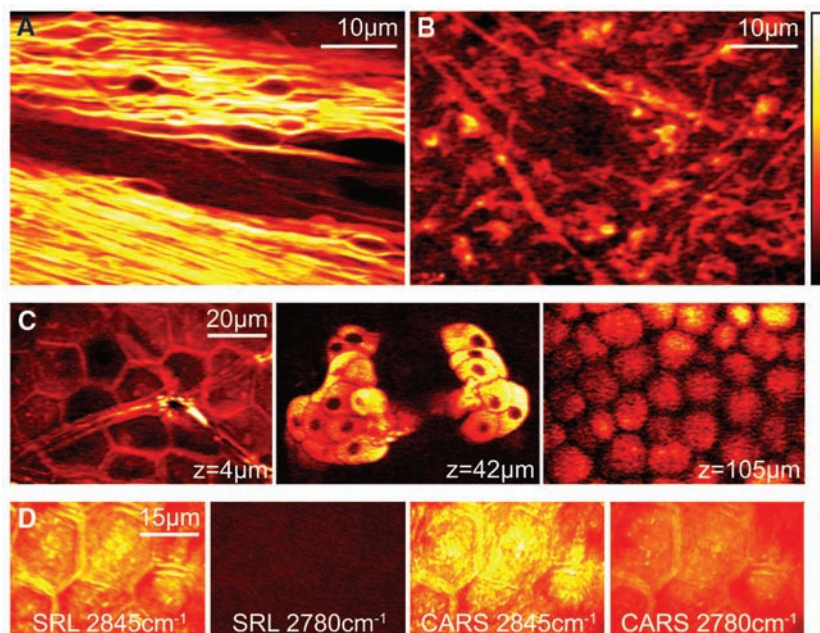
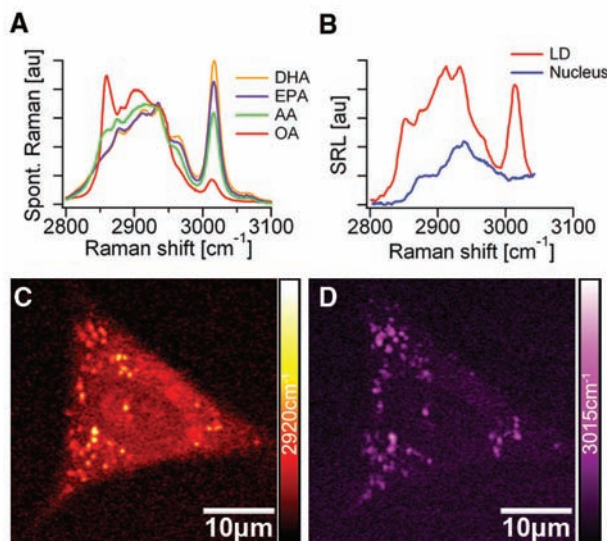


Fig. 3. SRL imaging of fresh mouse tissue. (A) Neuron bundles in corpus callosum of mouse brain imaged at 2845 cm^{-1} highlighting myelin sheaths rich in CH_2 . See movie in (18). (B) Epi-detected SRL CH_2 image acquired from thick brain tissue. (C) SRL CH_2 images of mouse ear skin in the same area at the indicated depths. From left to right: stratum corneum ($4\text{ }\mu\text{m}$), sebaceous gland ($42\text{ }\mu\text{m}$), and subcutaneous fat layer ($105\text{ }\mu\text{m}$). See movie in (18). (D) Comparison of SRL and CARS images of stratum corneum on (2845 cm^{-1}) and off (2780 cm^{-1}) the CH_2 resonance. Unlike CARS, SRL has no nonresonant background.

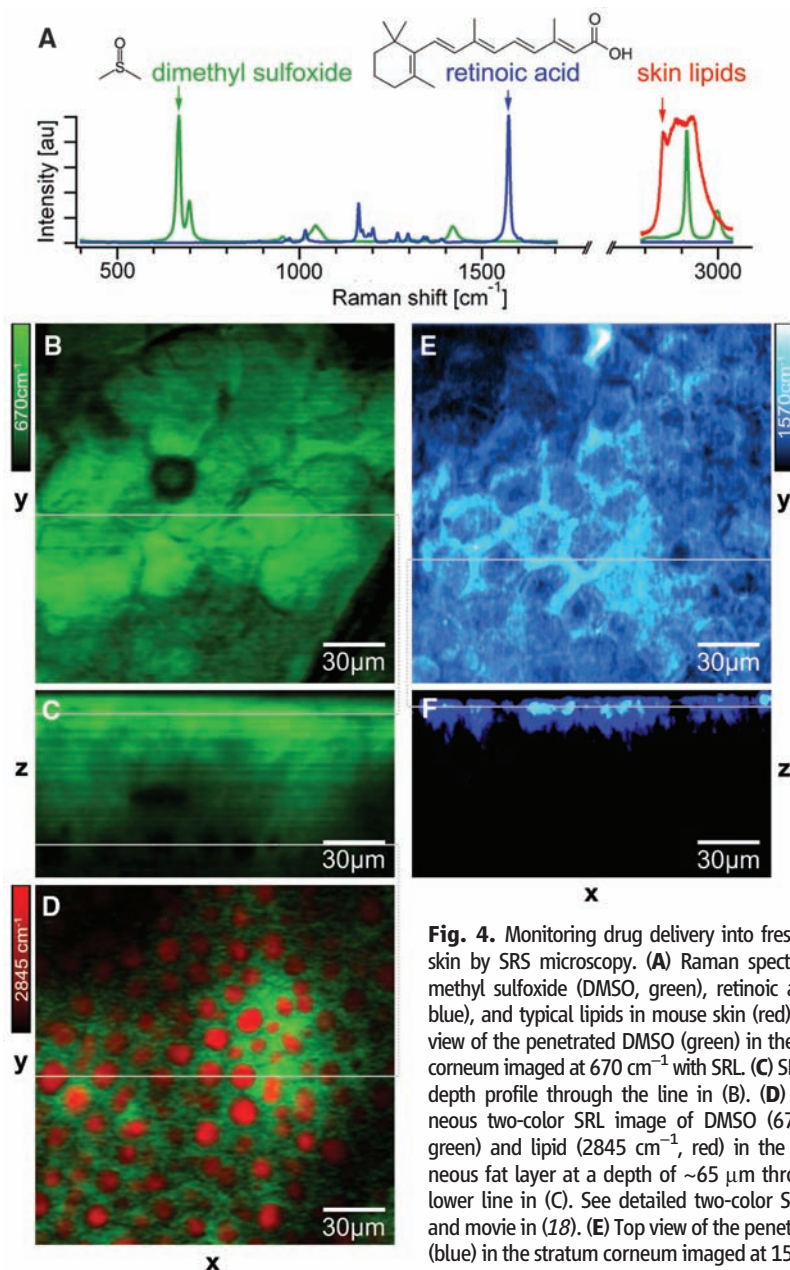


Fig. 4. Monitoring drug delivery into fresh mouse skin by SRS microscopy. (A) Raman spectra of dimethyl sulfoxide (DMSO, green), retinoic acid (RA, blue), and typical lipids in mouse skin (red). (B) Top view of the penetrated DMSO (green) in the stratum corneum imaged at 670 cm^{-1} with SRL. (C) SRL DMSO depth profile through the line in (B). (D) Simultaneous two-color SRL image of DMSO (670 cm^{-1} , green) and lipid (2845 cm^{-1} , red) in the subcutaneous fat layer at a depth of $\sim 65\text{ }\mu\text{m}$ through the lower line in (C). See detailed two-color SRL setup and movie in (18). (E) Top view of the penetrated RA (blue) in the stratum corneum imaged at 1570 cm^{-1} with SRL. (F) SRL RA depth profile through the line

in (E). SRS allows label-free 3D in situ visualization of two different drug-delivery pathways into the skin.

CH_2 stretching mode, the SRL signal vanishes completely, whereas the nonresonant CARS background still exhibits contrast that complicates image interpretation. We note that tissue autofluorescence does not interfere with the SRS. The absence of the nonresonant background in SRS reflects the major advantage over CARS imaging.

We also show the use of SRS to monitor drug delivery. Fluorescent labels are usually larger than drug molecules and may perturb their transport properties. Although confocal spontaneous Raman microscopy has been used to obtain longitudinal penetration profiles, the lateral distribution is often compromised due to the long pixel dwell times (29). Here we show the mapping of the distribution of two com-

pounds: dimethyl sulfoxide (DMSO), a skin-penetration enhancer (29); and retinoic acid (RA), which is used to treat acne, wrinkles, photoaging, and acute promyelocytic leukemia (30). According to Raman spectra (Fig. 4A), DMSO and RA have isolated vibrational resonances at 670 and 1570 cm^{-1} , respectively.

As a hydrophilic molecule, DMSO penetrates the skin via the protein phase, so the DMSO image in the stratum corneum (Fig. 4B) shows inverse contrast compared to the lipid image in Fig. 3C. A depth profile shows detectable DMSO over more than $60\text{ }\mu\text{m}$ (Fig. 4C), and the hydrophilic interaction with the tissue is confirmed in the subcutaneous fat layer. Simultaneous two-color imaging tuned into lipid and DMSO (18)

allows us to show that the DMSO is insoluble in the lipid structures (Fig. 4D). In contrast, RA, which is a hydrophobic molecule, penetrates via the lipid-rich intercellular space in the epidermis (Fig. 4, E and F) after ultrasonication of the tissue to enhance delivery (18). These results show that SRS offers a new approach for studying pharmacokinetics in situ. As a label-free and sensitive imaging modality, SRS microscopy allows mapping of molecular species in 3D and the ability to follow their dynamics in living cells and organisms based on the wealth of Raman spectroscopy.

References and Notes

1. C. V. Raman, K. S. Krishnan, *Nature* **121**, 711 (1928).
2. G. Turrell, J. Corset, *Raman Microscopy: Developments and Applications* (Academic Press, San Diego, 1996).
3. A. Zumbusch, G. R. Holtom, X. S. Xie, *Phys. Rev. Lett.* **82**, 4142 (1999).
4. C. L. Evans, X. S. Xie, *Annu. Rev. Anal. Chem.* **1**, 27 (2008).
5. N. Bloembergen, *Am. J. Phys.* **35**, 989 (1967).
6. R. W. Boyd, *Nonlinear Optics* (Academic Press, San Diego, 2003).
7. A. Einstein, *Phys. Z.* **18**, 121 (1917).
8. E. J. Woodbury, W. K. Ng, *Proc. Inst. Radio Eng.* **50**, 2367 (1962).
9. A. Owyong, *Opt. Commun.* **22**, 323 (1977).
10. B. F. Levine, C. V. Shank, J. P. Heritage, *IEEE J. Quantum Electron.* **15**, 1418 (1979).
11. M. D. Levenson, S. S. Kano, *Introduction to Nonlinear Laser Spectroscopy* (Academic Press, San Diego, 1988).
12. P. Kukura, D. W. McCamant, R. A. Mathies, *Annu. Rev. Phys. Chem.* **58**, 461 (2007).
13. W. Denk, J. H. Strickler, W. W. Webb, *Science* **248**, 73 (1990).
14. E. Ploetz, S. Laimgruber, S. Berner, W. Zinth, P. Gilch, *Appl. Phys. B Lasers Opt.* **87**, 389 (2007).
15. Y. Fu, H. F. Wang, R. Y. Shi, J. X. Cheng, *Opt. Exp.* **14**, 3942 (2006).
16. J. Ye, L. S. Ma, J. L. Hall, *J. Opt. Soc. Am. B* **15**, 6 (1998).
17. D. Fu et al., *Opt. Lett.* **32**, 2641 (2007).
18. Methods, additional results, and movies are available as supporting material on Science Online
19. E. O. Potma, W. P. de Boeij, D. A. Wiersma, *J. Opt. Soc. Am. B* **17**, 1678 (2000).
20. K. Ekvall et al., *J. Appl. Phys.* **87**, 2340 (2000).
21. Another spurious background signal can arise from two-color two-photon absorption of the pump and Stokes beams. See (17).
22. C. L. Evans et al., *Proc. Natl. Acad. Sci. U.S.A.* **102**, 16807 (2005).
23. F. Ganikhanov, C. L. Evans, B. G. Saar, X. S. Xie, *Opt. Lett.* **31**, 1872 (2006).
24. Y. R. Shen, *The Principle of Nonlinear Optics* (Wiley, New Jersey, 2003).
25. Subtle spectral differences between spontaneous Raman spectroscopy and SRS have been predicted theoretically. See (31).
26. J. X. Kang, *J. Membr. Biol.* **206**, 165 (2005).
27. C. Heinrich et al., *Opt. Exp.* **16**, 2699 (2008).
28. H. Wang, Y. Fu, P. Zickmund, R. Y. Shi, J. X. Cheng, *Biophys. J.* **89**, 581 (2005).
29. P. J. Caspers et al., *Pharm. Res.* **19**, 1577 (2002).
30. P. C. M. Van De Kerkhof et al., *J. Dermatolog. Treat.* **17**, 198 (2006).
31. P. Kukura, D. W. McCamant, R. A. Mathies, *J. Phys. Chem. A* **108**, 5921 (2004).
32. We thank C. Ackermann and S. Zhang for advice on skin imaging; S. Kesari, X. Xu and the MCB Harvard Mouse Facilities for providing mouse tissue; J. Grice and M. Roberts for the loan of a sonicator; and G. Young, X. Xu, M. Rückel, and P. Sims for helpful discussions. C.W.F. and B.G.S. thank Boehringer Ingelheim Fonds for a Ph.D. Fellowship and the Army Research Office for a National Defense Science and Engineering Graduate Fellowship, respectively. J.X.K. acknowledges support from the NIH (grant CA113605).

The Xie Group is grateful to the U.S. Department of Energy's Basic Energy Sciences program (DE-FG02-07ER15875) for supporting high-sensitivity Raman detection. The instrumentation development was supported by NSF (grant DBI-0649892), NIH Director's Pioneer Award (to X.S.X.), the Bill & Melinda Gates Foundation Gates Foundation, and Pfizer

Global Medical. Harvard University has filed a patent application based on this work.

Supporting Online Material

www.sciencemag.org/cgi/content/full/322/5909/1857/DC1
Materials and Methods

Figs. S1 to S6
Movies S1 to S3

10 September 2008; accepted 19 November 2008
10.1126/science.1165758

Leukemic Cells Create Bone Marrow Niches That Disrupt the Behavior of Normal Hematopoietic Progenitor Cells

Angela Colmone, Maria Amorim, Andrea L. Pontier, Sheng Wang, Elizabeth Jablonski, Dorothy A. Sipkins*

The host tissue microenvironment influences malignant cell proliferation and metastasis, but little is known about how tumor-induced changes in the microenvironment affect benign cellular ecosystems. Applying dynamic *in vivo* imaging to a mouse model, we show that leukemic cell growth disrupts normal hematopoietic progenitor cell (HPC) bone marrow niches and creates abnormal microenvironments that sequester transplanted human CD34⁺ (HPC-enriched) cells. CD34⁺ cells in leukemic mice declined in number over time and failed to mobilize into the peripheral circulation in response to cytokine stimulation. Neutralization of stem cell factor (SCF) secreted by leukemic cells inhibited CD34⁺ cell migration into malignant niches, normalized CD34⁺ cell numbers, and restored CD34⁺ cell mobilization in leukemic mice. These data suggest that the tumor microenvironment causes HPC dysfunction by usurping normal HPC niches and that therapeutic inhibition of HPC interaction with tumor niches may help maintain normal progenitor cell function in the setting of malignancy.

Hematopoietic progenitor cells (HPCs) home to and engraft in highly specific bone marrow (BM) microenvironments, or niches, that regulate their survival, proliferation, and differentiation (1, 2). These niches have been defined by the association of particular stromal cell types and by their elaboration or secretion of specific signaling molecules,

growth factors, and cytokines (3). At least two distinct HPC-supportive niches have been identified in the BM: an osteoblastic niche in which molecules including bone morphogenetic protein, osteopontin, angiopoietin-1, and Notch appear to play important regulatory roles; and a vascular niche that remains to be molecularly defined (4–8).

Although defects in hematopoiesis are frequently observed in patients with malignant involvement of the BM, the molecular bases of these phenomena, and whether they might reflect perturbations in HPC-supportive niches, are unknown. Suppression of normal hematopoiesis can occur in the setting of relatively low tumor burden and thus does not necessarily reflect anatomic “crowding out” of benign cells.

Using a severe combined immunodeficiency (SCID) mouse xenograft model of Nalm-6 pre-B acute lymphoblastic leukemia (ALL), we have shown that malignant cells metastasize to specific stromal cell–derived factor–1 (SDF-1)–positive vascular niches in the BM that overlap with perivascular HPC niches (9). To investigate whether benign and malignant cells compete for niche resources, we used real-time, *in vivo* confocal and multiphoton microscopy imaging approaches that allowed us to colocalize fluorescently labeled BM antigens with fluorescently labeled human CD34⁺ cells, which are highly enriched in HPCs, and fluorescent tumor cells (10). For intravenous transplant into mice, we harvested CD34⁺ cells from human cord blood and from the peripheral blood of human donors who had been treated

Department of Medicine, Section of Hematology/Oncology, The University of Chicago, 5841 South Maryland Avenue MC 2115, Chicago, IL 60637, USA.

*To whom correspondence should be addressed: E-mail: dsipkins@medicine.bsd.uchicago.edu

Fig. 1. Leukemia-induced changes in the BM microenvironment disrupt CD34⁺ cell homing. **(A)** Diagram of mouse calvarial BM vasculature. In control mice, CD34⁺ cells predominantly home to parasagittal sinusoidal vasculature. A major fraction of CD34⁺ cells engraft in this parasagittal region after homing, whereas other CD34⁺ cells migrate to more lateral osteoblastic and vascular niches. **(B)** SDF-1 (red) is highly expressed in the parasagittal sinusoidal region (CD34⁺ cell homing sites) of control mice. Nalm-6–GFP cells (green) preferentially home to and proliferate in this area, leading to marked down-regulation of SDF-1 expression, here shown at 35 days after Nalm-6–GFP engraftment. Central vein (cv) is labeled for orientation. **(C)** CD34⁺ cells (white) home to the SDF-1–positive parasagittal vascular niches in control mice. CD34⁺ cells aberrantly home to SDF-1–negative, lateral regions in tumor (green)–engrafted mice. Scale bars (B and C), 250 μ m.

